

Optical Engineering

OpticalEngineering.SPIEDigitalLibrary.org

Correction of axial position uncertainty and systematic detector errors in ptychographic diffraction imaging

Lars Loetgering
Max Rose
Kahraman Keskinbora
Margarita Baluktsian
Gül Dogan
Umut Sanli
Iuliia Bykova
Markus Weigand
Gisela Schütz
Thomas Wilhein

SPIE.

Lars Loetgering, Max Rose, Kahraman Keskinbora, Margarita Baluktsian, Gül Dogan, Umut Sanli, Iuliia Bykova, Markus Weigand, Gisela Schütz, Thomas Wilhein, "Correction of axial position uncertainty and systematic detector errors in ptychographic diffraction imaging," *Opt. Eng.* **57**(8), 084106 (2018), doi: 10.1117/1.OE.57.8.084106.

Correction of axial position uncertainty and systematic detector errors in ptychographic diffraction imaging

Lars Loetgering,^{a,*} Max Rose,^b Kahraman Keskinbora,^c Margarita Baluktsian,^c Gül Dogan,^c Umut Sanli,^c Iuliia Bykova,^c Markus Weigand,^c Gisela Schütz,^c and Thomas Wilhein^a

^aHochschule Koblenz, Institute for X-Optics, Remagen, Germany

^bDeutsches Elektronen-Synchrotron DESY, Hamburg, Germany

^cMax Planck Institute for Intelligent Systems, Stuttgart, Germany

Abstract. Ptychography is a diffraction imaging method that allows one to solve inverse problems in microscopy with the ability to retrieve information about and correct for systematic errors. Here, we propose techniques to correct for axial position uncertainty, detector point spread, and inhomogeneous detector response using ptychography's inherent self-calibration capabilities. The proposed methods are tested with visible light and x-ray experimental data. We believe that the results are important for precise calibration of ptychographic experimental setups and rigorous quantification of partially coherent beams by means of ptychography. © The Authors. Published by SPIE under a Creative Commons Attribution 3.0 Unported License. Distribution or reproduction of this work in whole or in part requires full attribution of the original publication, including its DOI. [DOI: [10.1117/1.OE.57.8.084106](https://doi.org/10.1117/1.OE.57.8.084106)]

Keywords: ptychography; detector characteristics; coherence; computational imaging.

Paper 180723 received May 18, 2018; accepted for publication Aug. 14, 2018; published online Aug. 31, 2018.

1 Introduction

Ptychographic coherent diffraction imaging (PCDI) is a scanning microscopy technique that has gained wide popularity during the last decade.^{1–3} Its ability to recover illumination and object information with phase contrast sensitivity without the need for sophisticated specimen preparation makes it suitable for both beam diagnostics^{4,5} and quantitative imaging^{6–9} in a variety of spectral ranges and experimental geometries.^{10–13} However, PCDI relies on accurate experimental calibration, and incorrect modeling of the data can lead to reconstruction artifacts. Here, we report on correction schemes to mitigate detector-sided systematic errors, namely axial position uncertainty, point spread, and inhomogeneous response. We derive theoretical models for the aforementioned systematic errors and present correction strategies to improve reconstruction quality. One result is that the effect of axial position uncertainty is to scale the estimated coordinates of each scan position. An algorithm is presented to detect and correct for axial position errors based on lateral position correction. A second result is that both point spread and inhomogeneous response of the detector can be mitigated by mixed state ptychography.¹⁴ The paper is organized as follows: Sec. 2 reviews details regarding PCDI and gives a theoretical description of the aforementioned systematic errors. Section 3 demonstrates experimental results on the classification and correction of axial position uncertainty and detector point spread. Concluding remarks are given in Sec. 4.

2 Methods

2.1 Ptychography

Under the thin object approximation,² the exit wave ψ downstream an object is modeled as the product of illumination P and object transmission O :

$$\psi_j(\mathbf{r}) = P(\mathbf{r})O(\mathbf{r} - \mathbf{t}_j), \quad j \in \{1, \dots, J\}, \quad (1)$$

where $\mathbf{r} \in \mathbb{R}^2$ denotes object coordinates, $\mathbf{t}_j \in \mathbb{R}^2$ is the translation vector of the j 'th scan position, and J is the total number of scan positions. The far-field diffraction intensities I are given as the modulus squared of the Fourier transform of the exit wave:

$$I(\mathbf{q}, \mathbf{t}_j) = |\mathcal{F}\{\psi_j(\mathbf{r})\}|^2, \quad (2)$$

where $\mathbf{q} \in \mathbb{R}^2$ denotes detector coordinates. In the case of partially coherent illumination, the model is generalized to incorporate coherence state mixtures,¹⁴ involving a set of coherent modes:

$$\psi_{m,j}(\mathbf{r}) = P_m(\mathbf{r})O(\mathbf{r} - \mathbf{t}_j), \quad m \in \{1, \dots, M\}, \quad (3)$$

which are propagated independently through the optical system and added incoherently upon detection, i.e.,

$$I(\mathbf{q}, \mathbf{t}_j) = \sum_m |\mathcal{F}\{\psi_{m,j}(\mathbf{r})\}|^2, \quad (4)$$

where the summation index corresponds to the m 'th mode in the orthogonal mode expansion of the illumination.¹⁵

Standard ptychography algorithms iterate between two constraints in reciprocal and real space. The reciprocal space constraint forces the iterate to comply with the measured intensities for each scan position, i.e.,

$$\tilde{\psi}_{m,j}^{n+1}(\mathbf{q}) = \frac{\sqrt{I(\mathbf{q}, \mathbf{t}_j)}}{\sqrt{\sum_{m'} |\tilde{\psi}_{m',j}^n(\mathbf{q})|^2 + \epsilon}} \tilde{\psi}_{m,j}^n(\mathbf{q}), \quad (5)$$

where n denotes iteration, $\epsilon > 0$ is a small constant preventing division by zero, and $\tilde{\psi}_{m,j}^n(\mathbf{q})$ is the Fourier transform of the m 'th exit surface mode at the j 'th object position. Scanning the object in overlapping regions provides ptychography with phase contrast sensitivity.² The overlap in scan positions

*Address all correspondence to: Lars Loetgering, E-mail: lars.loetgering@fulbrightmail.org

together with the factorization assumption in Eq. (1) gives the real space constraint, which is typically imposed iteratively via nonlinear optimization algorithms.^{2,16–18} In this report, we use the real space updates:

$$P_m^{n+1}(\mathbf{r}) = P_m^n(\mathbf{r}) + \beta \frac{O^{n*}(\mathbf{r} - \mathbf{t}_j)}{\max |O^n(\mathbf{r} - \mathbf{t}_j)|^2} (\psi_{m,j}^n(\mathbf{r}) - P_m^n(\mathbf{r}) O^n(\mathbf{r} - \mathbf{t}_j)) \quad (6)$$

and

$$O^{n+1}(\mathbf{r}) = O^n(\mathbf{r}) + \beta \frac{\sum_m P_m^{n*}(\mathbf{r} + \mathbf{t}_j)}{\max \sum_{m'} |P_{m'}^n(\mathbf{r} + \mathbf{t}_j)|^2} (\psi_{m,j}^n(\mathbf{r} + \mathbf{t}_j) - P_m^n(\mathbf{r} + \mathbf{t}_j) O^n(\mathbf{r})), \quad (7)$$

where $\beta = 0.5$ is a feedback parameter, P_m^{n+1} is the updated m 'th probe mode estimate, and O^{n+1} is the updated object estimate. The latter updates are adapted versions of the extended ptychographic iterative engine (ePIE) for the case of partially coherent illumination.^{14,19} Assuming quasi-monochromatic radiation, the reconstructed coherent modes of the probe relate to the mutual intensity, $J(\mathbf{r}_1, \mathbf{r}_2)$, via¹⁴

$$J(\mathbf{r}_1, \mathbf{r}_2) = \sum_m P_m^*(\mathbf{r}_1) P_m(\mathbf{r}_2). \quad (8)$$

The mutual intensity can be spectrally decomposed into¹⁵

$$J(\mathbf{r}_1, \mathbf{r}_2) = \sum_m \lambda_m \phi_m^*(\mathbf{r}_1) \phi_m(\mathbf{r}_2), \quad (9)$$

where the orthonormal modes ϕ_m are determined by the integral equation:

$$\int J(\mathbf{r}_1, \mathbf{r}_2) \phi_m^*(\mathbf{r}_1) d\mathbf{r}_1 = \lambda_m \phi_m(\mathbf{r}_2). \quad (10)$$

The eigenvalues λ_m define the purity:²⁰

$$\nu = \frac{\sqrt{\sum_m \lambda_m^2}}{\sum_m \lambda_m} \in [0,1], \quad (11)$$

which is used here as a measure for the degree of spatial coherence of the beam. The reconstructed probe modes are constrained to be proportional to the orthonormal modes in the spectral decomposition of the mutual intensity. Combining and discretizing Eqs. (8) and (9) lead to the matrix equation:²¹

$$\mathcal{P}\mathcal{P}^* = \Phi\Lambda\Phi^*, \quad (12)$$

where $\mathcal{P} = [P_{1,-}, P_M] \in \mathbb{C}^{N \times M}$ contains the probe modes along its columns, $\Phi = [\phi_{1,-}, \phi_M] \in \mathbb{C}^{N \times M}$ is orthonormal, $\Lambda \in \mathbb{R}^{M \times M}$ is diagonal containing the eigenvalues $\lambda_{1,-}, \lambda_M \geq 0$, and N is the total number of samples in the discretized beam. In practice, calculation of $\mathcal{P}\mathcal{P}^* \in \mathbb{C}^{N \times N}$ is computationally expensive and should be avoided. This can be achieved using the truncated singular value decomposition for the orthogonalization of the probe:²²

$$\mathcal{P} = \mathcal{U}\mathcal{S}\mathcal{V}^*, \quad (13)$$

where $\mathcal{U} \in \mathbb{C}^{N \times M}$, $\mathcal{S} \in \mathbb{R}^{M \times M}$, and $\mathcal{V} \in \mathbb{C}^{M \times M}$. Comparing

$$\mathcal{P}\mathcal{P}^* = \mathcal{U}\mathcal{S}^2\mathcal{U}^* \quad (14)$$

and Eq. (12) leads to the identities $\Phi = \mathcal{U}$ and $\Lambda = \mathcal{S}^2$. A set of orthogonalized probe modes \mathcal{P}_\perp is derived from the set of nonorthogonalized probe modes \mathcal{P} using the transformation:

$$\mathcal{P} \rightarrow \mathcal{P}_\perp = \mathcal{U}\mathcal{S}. \quad (15)$$

The latter step allows one to identify the orthogonalized set of probe modes with the orthogonal modes and their corresponding weights in the spectral decomposition of the mutual intensity, namely $\mathcal{P}_\perp = \Phi\Lambda^{1/2}$. The orthogonalization of the probe modes [Eq. (15)] does not have to be calculated at every iteration of the ptychographic algorithm. In the software implementation used here, the orthogonalization step is carried out every 10th iteration to save computational resources. The next sections discuss departures from the ideal experimental model discussed above and correction strategies.

2.2 Axial Position Correction

The first imperfection considered is axial misalignment of the object–detector distance z , which has been reported to cause nonuniqueness and artifacts in the reconstruction.^{23,24}

The effect of axial displacement of the detector is to scale the real space coordinates \mathbf{t}_j attributed to each object frame $O(\mathbf{r} - \mathbf{t}_j)$. Assuming far-field diffraction, the real space pixel size Δx and field of view L are given by $\Delta x = \lambda z/D$ and $L = \lambda z/\Delta q$, respectively, where D is the detector size and Δq is the detector pixel size. On an integer grid, a point at coordinate x is converted into dimensionless pixel coordinates $N = x/\Delta x$, where rounding is neglected. Then, the difference between the true pixel location, N_t , and the measured pixel location, N_m , is given by

$$\Delta N = N_m - N_t = \frac{xD}{\lambda(z + \Delta z)} - \frac{xD}{\lambda z} = -\frac{xD}{\lambda z} \frac{\Delta z}{z + \Delta z}. \quad (16)$$

From this, it follows that the coordinate error is proportional to the distance from the center of the coordinate system x and to the ratio $\Delta z/(z + \Delta z)$. The latter quantity can be approximated by $\Delta z/z$ assuming $|\Delta z| \ll z$. Equation (16) is illustrated in Fig. 1. The sign of Δz in Eq. (16) leads to contraction or inflation of the scan grid: If the measured object–detector distance z_m is larger than the ground truth object–detector distance z_t , i.e., $\Delta z = z_m - z_t > 0$, then $\Delta N < 0$ and the estimated lateral positions are contracted with respect to the actual scan grid. In the other case, when $z_m < z_t$, i.e., $\Delta z = z_m - z_t < 0$, then $\Delta N > 0$ and the estimated scan grid is inflated. The former case is shown on the left and the latter case is shown on the right for a concentric²⁵ and a Fermat scan grid,²⁶ respectively.

The proportionality of ΔN and x in Eq. (16) causes variable lateral position error that is most pronounced at the extremal points of the scan grid. Therefore, detector position uncertainty may be detected by the use of lateral position correction algorithms.^{27–29} In this report, we use a random walk lateral position correction scheme similar to algorithms

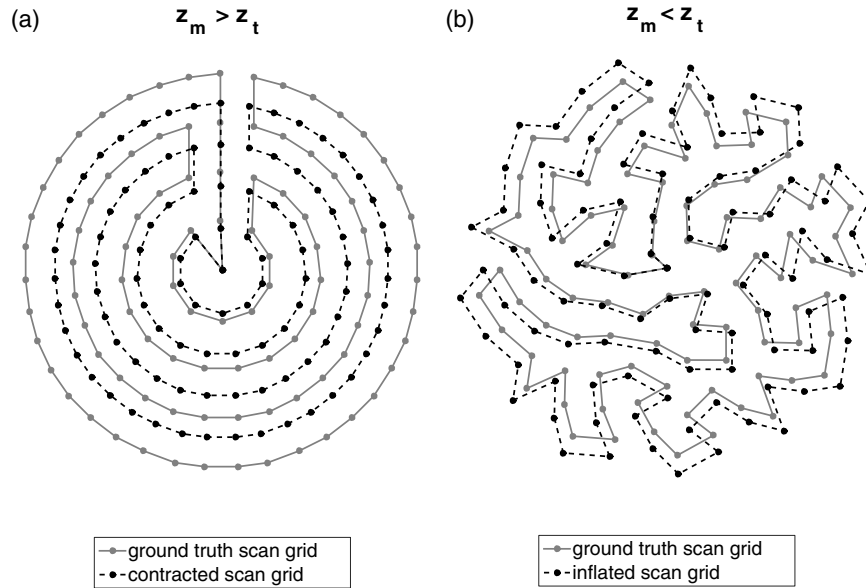


Fig. 1 Scan grid distortion as a consequence of axial detector position uncertainty. (a) If the measured object-detector distance z_m is larger than the ground truth z_t , the interpolated scan grid appears contracted as compared to the true scan grid, as shown for the case of a concentric scan grid. (b) The converse case, $z_m < z_t$, is depicted for the case of a Fermat spiral scan grid.

reported previously.^{29,30} In our scheme, no underlying annealing schedule or drift model is assumed. At every iteration, the random walk position correction performs the following steps: (1) For the j 'th position obtain unshifted and shifted exit wave modes, where the shift of the latter is given by ± 1 pixel in both lateral directions. (2) Update exit wave modes according to Eq. (5) and calculate the error metric:

$$e_j = \sum_m \int |\psi_{m,j}^{n+1} - \psi_{m,j}^n|^2 d\mathbf{r} \quad (17)$$

for the j 'th position. Equation (3) shows that if $e_{j,s} < c e_{j,u}$, where $e_{j,s}$ and $e_{j,u}$ are the errors of the shifted and unshifted exit wave modes, respectively, then the j 'th position is replaced by the shifted position. The constant $c < 1$ prevents premature position updates. In this report, we use $c = 0.95$.

2.3 Partial Spatial Coherence as a Convolution Operation

Assuming partial spatial coherence (PSC), the far-field diffraction intensity is given by

$$I^{\text{psc}}(\mathbf{q}, \mathbf{t}) = \int J(\mathbf{r}_1, \mathbf{r}_2, \mathbf{t}) \exp\left(-j2\pi \frac{(\mathbf{r}_2 - \mathbf{r}_1) \cdot \mathbf{q}}{\lambda z}\right) d\mathbf{r}_1 d\mathbf{r}_2, \quad (18)$$

where $J(\mathbf{r}_1, \mathbf{r}_2, \mathbf{t})$ is the mutual intensity in the object plane.³¹ For a Schell model field, the mutual intensity can be written as follows:

$$J(\mathbf{r}_1, \mathbf{r}_2, \mathbf{t}) = \psi(\mathbf{r}_1, \mathbf{t}) \psi^*(\mathbf{r}_2, \mathbf{t}) \mu(\mathbf{r}_2 - \mathbf{r}_1), \quad (19)$$

where μ is the complex coherence factor.³² Changing to centered coordinates $\bar{\mathbf{r}} = (\mathbf{r}_1 + \mathbf{r}_2)/2$ and $\Delta\mathbf{r} = \mathbf{r}_2 - \mathbf{r}_1$, the partially coherent diffraction intensity is given by³³⁻³⁵

$$I^{\text{psc}}(\mathbf{q}, \mathbf{t}) = \int \psi\left(\bar{\mathbf{r}} - \frac{\Delta\mathbf{r}}{2}, \mathbf{t}\right) \psi^*\left(\bar{\mathbf{r}} + \frac{\Delta\mathbf{r}}{2}, \mathbf{t}\right) \mu(\Delta\mathbf{r}) \times \exp\left(-j2\pi \frac{\Delta\mathbf{r} \cdot \mathbf{q}}{\lambda z}\right) d\bar{\mathbf{r}} d\Delta\mathbf{r}. \quad (20)$$

Using the autocorrelation and convolution theorems for Fourier transforms, this is equivalent to

$$I^{\text{psc}}(\mathbf{q}, \mathbf{t}) = I^c(\mathbf{q}, \mathbf{t}) \otimes \tilde{\mu}(\mathbf{q}), \quad (21)$$

where \otimes denotes convolution and

$$I^c(\mathbf{q}, \mathbf{t}) = \int \psi\left(\bar{\mathbf{r}} - \frac{\Delta\mathbf{r}}{2}, \mathbf{t}\right) \psi^*\left(\bar{\mathbf{r}} + \frac{\Delta\mathbf{r}}{2}, \mathbf{t}\right) \times \exp\left(-j2\pi \frac{\Delta\mathbf{r} \cdot \mathbf{q}}{\lambda z}\right) d\bar{\mathbf{r}} d\Delta\mathbf{r} \quad (22)$$

is the the coherent diffraction intensity. Equation (21) is Schell's theorem, which states that, given a complex coherence factor that is only a function of distance, the partially coherent diffraction intensity is equal to the coherent diffraction intensity convolved with the Fourier transform of the complex coherence factor.³⁵

2.4 Detector Point Spread as a Convolution Operation

If the detector is subject to point spread, the contrast in the diffraction pattern is reduced. In the ideal case, the detector discretely samples the diffraction intensity. In practice, the measured data on each pixel is integrated over a finite area. It is now shown that the integration over a finite pixel area can be modeled as a convolution operation, where only the one-dimensional case is derived. The extension to two dimensions is straightforward. The integrated intensity I^{int} is given by

$$I^{\text{int}}(q) = \int_{-\frac{\Delta q}{2}}^{\frac{\Delta q}{2}} I(q-p) dp, \quad (23)$$

where Δq is the pixel size of the detector. Fourier transformation of the latter expression with respect to q and changing orders of integration leads to

$$\tilde{I}^{\text{int}}(f_q) = \tilde{I}(f_q) \int_{-\frac{\Delta q}{2}}^{\frac{\Delta q}{2}} \exp(-i2\pi f_q p) dp = \tilde{I}(f_q) \tilde{PSF}(f_q), \quad (24)$$

where f_q is the Fourier conjugate variable to the detector coordinate q and

$$\begin{aligned} \tilde{PSF}(f_q) &= \int_{-\frac{\Delta q}{2}}^{\frac{\Delta q}{2}} \exp(-i2\pi f_q p) dp = \Delta q \frac{\sin(\pi \Delta q f_q)}{\pi \Delta q f_q} \\ &= \Delta q \text{sinc}(\Delta q f_q) \end{aligned} \quad (25)$$

is the transfer function of the detector. Inverse Fourier transform Eq. (24) to get

$$I^{\text{int}}(q) = I(q) \otimes PSF(q), \quad (26)$$

where

$$PSF(q) = \text{rect}\left(\frac{q}{\Delta q}\right) = \begin{cases} 1, & \text{if } |q| < \Delta q/2 \\ 0, & \text{else} \end{cases} \quad (27)$$

is the point spread function of the detector. The latter model for the point spread includes only the effect of area integration of the intensity incident of the detector. Other effects may additionally broaden the point spread function but depend on the electronic architecture of the detector at hand. Charge-coupled devices, for instance, may exhibit a broadened point spread due to tunneling between neighboring potential wells and charge diffusion during readout.^{36,37} The main point of this section is that the detector point spread may be modeled as a convolution operation on a diffraction intensity, as described by Eq. 26.

2.5 Partial Spatial Coherence versus Detector Point Spread Ambiguity

If both partial coherence and detector point spread are non-negligible, the observed diffraction intensity is given by

$$I(q, t) = I^c(q, t) \otimes \tilde{\mu}(q) \otimes PSF(q). \quad (28)$$

Under the above discussed approximations (Schell model beam and space-invariant detector point spread), ptychography's capability to reconstruct individual terms in the orthogonal mode decomposition has principally no means to distinguish the effects of partial coherence and detector point spread. However, it can be tested whether the terms in the orthogonal mode decomposition are due to partial coherence or detector point spread by changing the coherence defining aperture of the optical system. This is demonstrated in Sec. 3.2.

2.6 Mixed-State Ptychography in the Presence of Inhomogeneous Detector Response

In Ss. 2.2 and 2.4, it was discussed that the effect of PSC (for the case of a Schell model fields) and a space invariant detector point spread are mathematically modeled through a convolution operation with an a priori unknown kernel. Instead of estimating the kernel, the mixed state formalism allows one to incorporate convolution effects such as partial coherence,^{14,38} sample vibrations,^{39,40} stage movement during exposure^{41,42} (fly scan effects), and point spread of the detector^{14,40} into a mixed state probe. Mathematically, this is justified by Mercer's theorem, which states that a non-negative definite, hermitian, and square integrable kernel may be decomposed into a series of orthogonal modes.⁴³ A general cross-spectral density satisfies the latter conditions,¹⁵ including the special case of Schell model fields. In addition, it was observed that the mixed state algorithm can mitigate static detector imperfections such as inhomogeneous response.³⁸ It is easily seen that an inhomogeneous detector response obeys the conditions for Mercer's theorem to apply. Let a detector response be given by a real-valued function:

$$T(q) = \int T(q, q') \delta(q - q') dq' \in [0, 1]. \quad (29)$$

The hermiticity $T(q, q') = T^*(q', q)$ follows from the fact that T is real valued and diagonal. Further T is square integrable since it is bounded by 1 and nonzero only over a finite domain. Finally, it is non-negative definite since

$$\begin{aligned} &\int f^*(q) T(q, q') \delta(q - q') f(q') dq dq' \\ &= \int T(q, q') |f(q)|^2 dq \geq 0 \end{aligned} \quad (30)$$

for arbitrary functions $f(q)$. This suggests that Mercer's expansion may be used to correct for static detector imperfections.

3 Experimental Results

3.1 Detection and Correction of Axial Detector Position

To test the effect of axial detector position uncertainty, a visible light ptychographic scan was acquired. In the experiment, a He-Ne laser beam ($\lambda = 682.8$ nm) was focused onto a 12 bit CMOS detector (IDS UI-3370CP-M-GL, 2048×2048 pixel, $5.5 \mu\text{m}$ pixel size) by a lens with a focal length of 100 mm, as depicted in Fig. 2(a). The object was placed a distance of 41 mm downstream the lens and $z_t = 59$ mm upstream the detector. Under the paraxial approximation in this configuration, the detector measures the scaled Fourier transform of the exit wave behind the object emulating far-field diffraction.⁴⁴ The probe was approximately Gaussian with a standard deviation of $\sigma = 110 \mu\text{m}$ as calculated after reconstruction by⁴⁵

$$\sigma^2 = \langle (r - \langle r \rangle)^2 \rangle = \frac{\int r^2 |P(r)|^2 dr}{\int |P(r)|^2 dr} - \left(\frac{\int r |P(r)|^2 dr}{\int |P(r)|^2 dr} \right)^2, \quad (31)$$

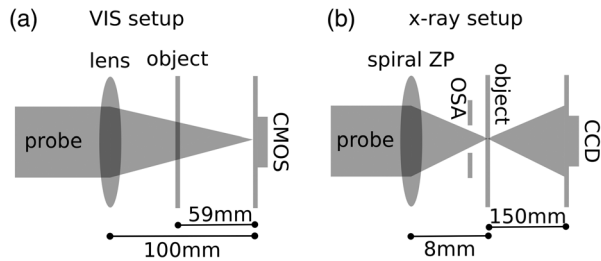


Fig. 2 (a) Visible light setup. Under the paraxial approximation, the detector measures the scaled Fourier transform of the illuminated object patch. (b) X-ray setup. The sample is illuminated critically by a vortex beam generated by a spiral zone plate. VIS, visible light detectors (CMOS and CCD); ZP, zone plate; OSA, order sorting aperture.

corresponding to a full-width at half-maximum (FWHM) of $259\ \mu\text{m}$. Reconstructions were carried out using an ePIE algorithm¹⁹ with the random walk position correction scheme described in Sec. 2.2 for distances $z_m = 50, 59, 62\ \text{mm}$, as shown in Fig. 3. It is seen that for $z_m < z_t$ (panel a) and for $z_m > z_t$ (panel c), the initial scan grids are inflated and contracted, respectively, as compared to the corrected scan grids. The scaling of the corrected scan grids with respect to the initial scan grid is in agreement with Eq. (16) and may be used to correct for axial position uncertainty. This step may be automated or carried out manually as done here.

3.2 Detector Point Spread and Static Detector Imperfections

To test whether the coherent mode structure of the illuminating beam can be attributed to PSC or detector point spread, experiments were carried out at the MAXYMUS end station

at the UE46-PGM2 beam line at the BESSY II synchrotron radiation facility.⁴⁶ A kinoform spiral zone plate of $32\ \mu\text{m}$ diameter and $400\ \text{nm}$ outer zone width was placed $3\ \text{m}$ downstream crossed exit slits to generate a charge one vortex beam with a spot size of $1.5\ \mu\text{m}$ to critically illuminate a binary test target at a photon energy of $800\ \text{eV}$. The experimental setup is depicted in Fig. 2(b). The region of interest on the test target was $\sim 6\ \mu\text{m}$ in each lateral dimension with a scan step size of $150\ \text{nm}$. The high linear overlap⁴⁷ of 90% ensured stable recovery of the higher coherent mode structure ($m > 1$) of the beam. A total of 1600 diffraction patterns were recorded on a CCD (cropped to 128×128 pixel, $48\text{-}\mu\text{m}$ pixel size) placed $15\ \text{cm}$ downstream the object resulting in a real space pixel size and field of view per object patch of $\Delta x = 38\ \text{nm}$ and $L = 4.8\ \mu\text{m}$, respectively.

The ptychographic reconstructions are shown in Fig. 4 for exit slit sizes of $10\ \mu\text{m} \times 10\ \mu\text{m}$ (top) and $20\ \mu\text{m} \times 20\ \mu\text{m}$ (bottom). For both exit slit openings, 1000 iterations were carried out with one (a, d) and nine (b, c, e, f) probe modes, four of which are shown (c, f). For the single mode reconstruction, the objects show artifacts at the outer region indicating that the tails of the probe were not reconstructed properly. For the multimode reconstruction, both objects show stronger similarity than for the single-mode reconstruction. Closer inspection of the multimode probe structure reveals that the degree of coherence did not significantly change between the two scans. The beam purities for the $10\ \mu\text{m} \times 10\ \mu\text{m}$ and $20\ \mu\text{m} \times 20\ \mu\text{m}$ slits are 63.9% and 60.5%, respectively. If partial coherence had been the cause for the coherent mode structure of the probe, then increasing the slit size by a factor of 2 would have resulted approximately in a twofold decrease in beam purity. From this, we conclude that the probe mode structure can mainly be

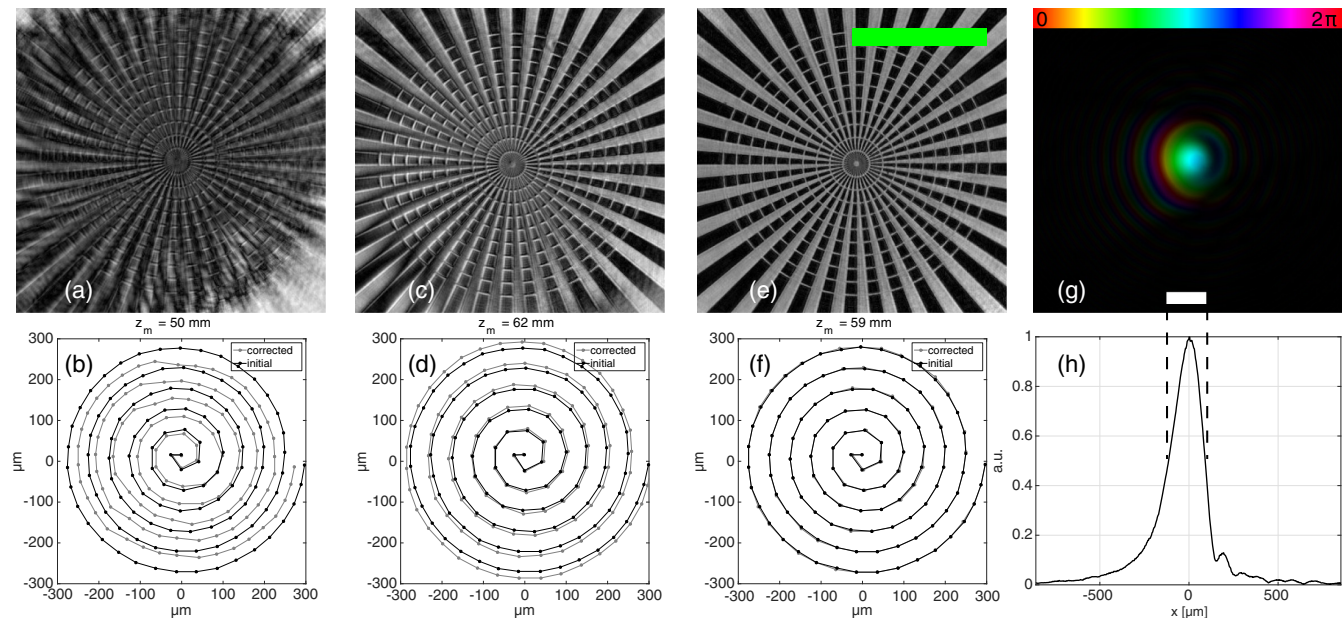


Fig. 3 Effect of axial detector misplacement. The reconstructed objects and scan grids for $z_m = 50, 62, 59\ \text{mm}$ are shown from left to right. Incorrect object–detector distances lead to scaled coordinate grids as predicted by Eq. (16) and artifacts in the object reconstruction (a–d). For the correct object–detector distance of $z_t = 59\ \text{mm}$, the corrected scan grid complies with the initial encoder values (e, f). The reconstructed probe in the object plane is shown for the correct object–detector distance (g, h). Hue (colored bar) and brightness are encoded as phase and intensity, respectively. The green and white scale bars show 500 and $259\ \mu\text{m}$ (FWHM), respectively.

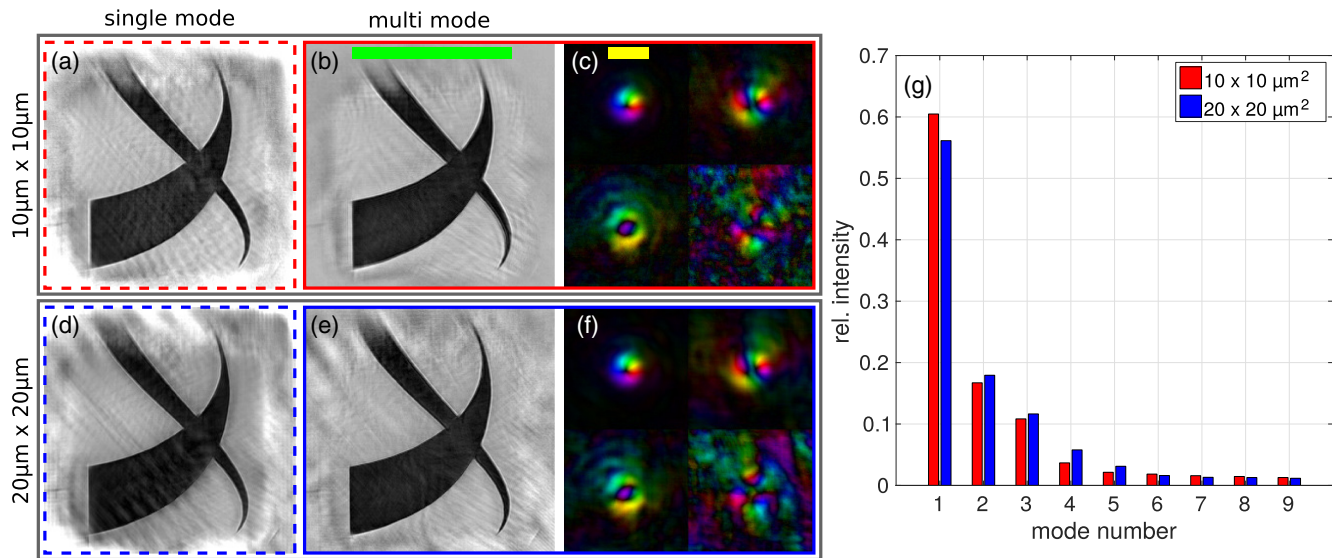


Fig. 4 (a, d) Single-mode reconstructions. Multimode reconstructed object and probe mode structure for exit slit sizes of $10\ \mu\text{m} \times 10\ \mu\text{m}$ and $20\ \mu\text{m} \times 20\ \mu\text{m}$ are shown in panels (b, c) and (e, f), respectively. Only the first four out of nine modes used in the probe model are shown. (g) The relative intensity of the individual probe modes for both scans is depicted on the right. The green and yellow scale bars show 5.8 and $1.5\ \mu\text{m}$, respectively.

attributed to detector point spread and static detector imperfections.

4 Conclusion

We have discussed two common detector-sided errors relevant in ptychographic diffraction imaging. The first error, axial misalignment, causes scaling of the correct lateral scan positions. It was shown that lateral position correction algorithms can be used to detect and correct for axial position uncertainty. The second detector-sided error discussed was detector point spread. We showed that this error can be identified by changing the spatial coherence defining element in the optical system, here the exit slit of a synchrotron beam line. If a change in exit slit size causes no response in the coherent mode structure of the illumination beam, the decreased diffraction pattern contrast can be attributed to detector point spread and static detector imperfections rather than PSC. However, while detector point spread is not attributable to decoherence in the beam, spectral mode decomposition, typically used for the representation of partially coherent beams, can be used to increase ptychographic reconstruction quality in the presence of detector point spread. Not shown in this work are initial tests on deconvolution strategies that we found to be less robust as compared to the mixed state algorithm. We believe that this is due to the dependence of the particular deconvolution ansatz on the specific underlying model. By contrast, the mixed state algorithm is conveniently applied since no *a priori* model of the detector error is required. Work on deconvolution of ptychographic data with explicit recovery of the detector point spread may be found elsewhere.⁴⁸ We believe that the results presented are important for improving reconstructions as well as rigorous quantification of partially coherent beams by means of ptychography.

Disclosures

The authors declare no conflicts of interest.

Acknowledgments

L. L. gratefully acknowledges help from D. Treffer in collecting the Siemens star data set and thanks I. Besedin for useful discussions. Part of the content of this paper was presented at the SPIE Computational Optics 2018 Conference (contribution 10694-9).

References

1. J. M. Rodenburg, A. C. Hurst, and A. G. Cullis, "Transmission microscopy without lenses for objects of unlimited size," *Ultramicroscopy* **107**(2–3), 227–231 (2007).
2. P. Thibault et al., "High-resolution scanning x-ray diffraction microscopy," *Science* **321**(5887), 379–382 (2008).
3. F. Pfeiffer, "X-ray ptychography," *Nat. Photonics* **12**(1), 9–17 (2018).
4. A. Schropp et al., "Full spatial characterization of a nanofocused x-ray free-electron laser beam by ptychographic imaging," *Sci. Rep.* **3**, 1633 (2013).
5. J. Vila-Comamala, A. Sakdinawat, and M. Guizar-Sicairos, "Characterization of x-ray phase vortices by ptychographic coherent diffractive imaging," *Opt. Lett.* **39**(18), 5281–5284 (2014).
6. N. Anthony et al., "A direct approach to in-plane stress separation using photoelastic ptychography," *Sci. Rep.* **6**, 1–10 (2016).
7. P. Ferrand et al., "Quantitative imaging of anisotropic material properties with vectorial ptychography," *Opt. Lett.* **43**(4), 763–766 (2018).
8. J. Deng et al., "X-ray ptychographic and fluorescence microscopy of frozen-hydrated cells using continuous scanning," *Sci. Rep.* **7**(1), 1–10 (2017).
9. M. Rose et al., "Quantitative ptychographic bio-imaging in the water window," *Opt. Express* **26**(2), 1237–1254 (2018).
10. D. F. Gardner et al., "High numerical aperture reflection mode coherent diffraction microscopy using off-axis apertured illumination," *Opt. Express* **20**(17), 19050–19059 (2012).
11. P. Li and A. M. Maiden, "Ten implementations of ptychography," *J. Microsc.* **269**(3), 187–194 (2018).
12. L. Valzania et al., "Terahertz ptychography," *Opt. Lett.* **43**(3), 543–546 (2018).
13. P. Helfenstern et al., "Beam drift and partial probe coherence effects in EUV reflective-mode coherent diffractive imaging," *Opt. Express* **26**(9), 12242–12256 (2018).
14. P. Thibault and A. Menzel, "Reconstructing state mixtures from diffraction measurements," *Nature* **494**(7435), 68–71 (2013).
15. E. Wolf, "New theory of partial coherence in the space-frequency domain. Part I: spectra and cross spectra of steady-state sources," *J. Opt. Soc. Am.* **72**(3), 343–351 (1982).
16. P. Thibault and M. Guizar-Sicairos, "Maximum-likelihood refinement for coherent diffractive imaging," *New J. Phys.* **14**(6), 063004 (2012).

17. S. Marchesini et al., "Augmented projections for ptychographic imaging," *Inverse Probl.* **29**(11), 115009 (2013).
18. A. Maiden, D. Johnson, and P. Li, "Further improvements to the ptychographical iterative engine," *Optica* **4**(7), 736–745 (2017).
19. A. M. Maiden and J. M. Rodenburg, "An improved ptychographical phase retrieval algorithm for diffractive imaging," *Ultramicroscopy* **109**(10), 1256–1262 (2009).
20. M. A. Alonso, "Wigner functions in optics: describing beams as ray bundles and pulses as particle ensembles," *Adv. Opt. Photonics* **3**(4), 272–365 (2011).
21. H. M. Ozaktas, "Linear algebraic theory of partial coherence: discrete fields and measures of partial coherence," *J. Opt. Soc. Am. A* **19**(8), 1563–1571 (2002).
22. L. Loetgering et al., "Data compression strategies for ptychographic diffraction imaging," *Adv. Opt. Technol.* **6**(6), 475–483 (2017).
23. N. Burdet et al., "Observations of artefacts in the x-ray ptychography method," *Opt. Express* **22**(9), 10294–10303 (2014).
24. J. Dou et al., "Iterative autofocusing strategy for axial distance error correction in ptychography," *Opt. Lasers Eng.* **98**, 56–61 (2017).
25. M. Dierolf et al., "Ptychographic coherent diffractive imaging of weakly scattering specimens," *New J. Phys.* **12**(3), 035017 (2010).
26. X. Huang et al., "Optimization of overlap uniformness for ptychography," *Opt. Express* **22**, 12634–12644 (2014).
27. M. Guizar-Sicairos and J. R. Fienup, "Phase retrieval with transverse translation diversity: a nonlinear optimization approach," *Opt. Express* **16**(10), 7264–7278 (2008).
28. G. Zheng, R. Horstmeyer, and C. Yang, "Wide-field, high-resolution Fourier ptychographic microscopy," *Nat. Photonics* **7**(9), 739–745 (2013).
29. M. Beckers et al., "Drift correction in ptychographic diffractive imaging," *Ultramicroscopy* **126**, 44–47 (2013).
30. A. M. Maiden et al., "An annealing algorithm to correct positioning errors in ptychography," *Ultramicroscopy* **120**, 64–72 (2012).
31. D. Paganin, *Coherent X-Ray Optics*, 1st ed., Oxford University Press, Oxford (2006).
32. M. Born and E. Wolf, *Principles of Optics*, 7th ed., Cambridge University Press, Cambridge (1999).
33. J. M. Rodenburg and R. H. T. Bates, "The theory of super-resolution electron microscopy via Wigner-distribution deconvolution," *Philos. Trans. R. Soc. London Ser. A* **339**(1655), 521–553 (1992).
34. R. Horstmeyer and C. Yang, "A phase space model of Fourier ptychographic microscopy," *Opt. Express* **22**(1), 338–358 (2014).
35. J. W. Goodman, *Statistical Optics*, 2nd ed., Wiley, New York (2015).
36. H. Du and K. J. Voss, "Effects of point-spread function on calibration and radiometric accuracy of CCD camera," *Appl. Opt.* **43**, 665–670 (2004).
37. D. J. Brady, *Optical Imaging and Spectroscopy*, 1st ed., John Wiley and Sons, Hoboken, New Jersey (2009).
38. B. Enders et al., "Ptychography with broad-bandwidth radiation," *Appl. Phys. Lett.* **104**(17), 171104 (2014).
39. J. N. Clark et al., "Dynamic imaging using ptychography," *Phys. Rev. Lett.* **112**(11), 1–5 (2014).
40. B. Enders, "Development and application of decoherence models in ptychographic diffraction imaging," PhD Thesis, Technical University Munich (2016).
41. J. N. Clark et al., "Continuous scanning mode for ptychography," *Opt. Lett.* **39**(20), 6066–6069 (2014).
42. P. M. Pelz et al., "On-the-fly scans for x-ray ptychography," *Appl. Phys. Lett.* **105**(25), 251101 (2014).
43. G. Gbur, *Mathematical Methods for Optical Physics and Engineering*, 1 ed., Cambridge University Press, New York (2011).
44. J. W. Goodman, *Introduction to Fourier Optics*, 3rd ed., Roberts and Company Publishers, Eaglewood (2004).
45. R. Bracewell, *The Fourier Transform and Its Applications*, 3rd ed., McGraw-Hill, New York (1999).
46. R. Follath et al., "The x-ray microscopy beamline UE46-PGM2 at BESSY," *AIP Conf. Proc.* **1234**(1), 323–326 (2010).
47. O. Bunk et al., "Influence of the overlap parameter on the convergence of the ptychographical iterative engine," *Ultramicroscopy* **108**, 481–487 (2008).
48. M. Odstrcil et al., "Ptychographic imaging with a compact gas-discharge," *Opt. Lett.* **40**(23), 5574–5577 (2015).

Lars Loetgering is currently enrolled as a PhD student at the Institute of X-Optics at the University of Applied Science, Koblenz, and Technical University Berlin. His research interests include computational imaging, ptychography, and phase retrieval.

Max Rose is PhD student at Deutsches Elektronen-Synchrotron Hamburg in the group of I. A. Vartanyants. His research interests include coherent x-ray diffraction imaging with phase retrieval and ptychography using synchrotron and x-ray free-electron laser sources.

Kahraman Keskinbora is currently leading the Micro/Nano Optics Group in the Department of Modern Magnetic Systems at Max-Planck-Institute for Intelligent Systems in Stuttgart. His research is focused on developing novel nanofabrication routes for innovative, high-efficiency and high-resolution x-ray optics using direct-write lithography techniques. The optics that he and his team develop are routinely used at the scanning transmission x-ray microscopy and soft x-ray ptychography beamline MAXYMUS at BESSY II.

Margarita Baluksian is a PhD student in the Micro/Nano Optics Group under the Department of Modern Magnetic Systems of the Max Planck Institute for Intelligent Systems in Stuttgart. In 2014, she graduated from the University of Stuttgart with a masters degree in physics. During her masters thesis and in the subsequent research stay at Oklahoma University in Norman in 2015, she was working in the field of atomic and optical physics. Since 2015, she works on the development, fabrication, and application of novel x-ray optics within the scope of her PhD thesis for various scientific needs.

Gül Dogan is currently a student associate in Kahraman Keskinbora's group in the Department of Modern Magnetic Systems at Max-Planck-Institute for Intelligent Systems in Stuttgart.

Umut Sanli is currently a PhD candidate at the Max Planck Institute for Intelligent Systems. His PhD research is focused on developing x-ray optics using innovative approaches for advancing x-ray microscopy. He is skilled in various nanoengineering and characterization techniques including atomic layer deposition, focused ion beam lithography, multiphoton lithography, microscopy, and spectroscopy using electrons and x-rays.

Iuliia Bykova is a PhD student in Max Planck Institute for Intelligent Systems in the group of Professor Schütz. Her research interests include soft x-ray microscopy and ptychography with magnetic and chemical contrast.

Markus Weigand is part of the Department of Modern Magnetic Systems at the Max-Planck-Institute for Intelligent Systems, leading the x-ray Microscopy Group. He is working locally at the BESSY II synchrotron operated by the Helmholtz-Zentrum Berlin as beamline/endstation scientist for the MAXYMUS x-ray microscope. His research is focused on implementing and improving advanced imaging methods such as ptychography or pump-and-probe microscopy.

Gisela Schütz is a director at the Max Planck Institute for Intelligent Systems. Her research interests cover the application of synchrotron radiation in x-ray spectroscopy and microscopy and the development of advanced spintronic/magnonic systems and new supermagnets.

Thomas Wilhein is a professor at the University of Applied Science, Koblenz. His research interests include high-resolution x-ray imaging with laboratory and synchrotron radiation sources.